Article

Antiferroelectric Phase Transition in a Proton-Transfer Salt of Squaric Acid and 2,3-Dimethylpyrazine

Jeff Lengyel, Xiaoping Wang, Eun Sang Choi, Tiglet Besara, Rico U Schönemann,
Sanath Kumar Ramakrishna, Jade Holleman, Avery L. Blockmon, Kendall D Hughey,
Tianhan Liu, Jacob Hudis, Drake Beery, Luis Balicas, Stephen A. McGill, Kenneth
Hanson, Janice L Musfeldt, Theo Siegrist, Naresh Dalal, and Michael Shatruk

Just Accepted

Antiferroelectric Phase Transition in a Proton-Transfer Salt of Squaric Acid and 2,3-Dimethylpyrazine

Jeff Lengyel,[a] Xiaoping Wang,[b] Eun Sang Choi,[c] Tiglet Besara,[c,#] Rico U. Schönemann,[c] Sanath Kumar Ramakrishna,[a,c] Jade Holleman,[c,d] Avery L. Blockmon,[e] Kendall D. Hughey,[e] Tianhan Liu,[d] Jacob Hudis,[d] Drake Beery,[a] Luis Balicas,[c,d] Stephen A. McGill,[c] Kenneth Hanson,[a] Janice L. Musfeldt,[e,f] Theo Siegrist,[c,g] Naresh Dalal,[a,c,*] Michael Shatruk[a,*]

[a] Department of Chemistry and Biochemistry, Florida State University, 95 Chieftan Way, Tallahassee, FL 32306, USA

[b] Neutron Scattering Division, Neutron Sciences Directorate, Oak Ridge National Laboratory, Oak Ridge, TN 37831, USA

[c] National High Magnetic Field Laboratory, 1800 E Paul Dirac Dr, Tallahassee, FL 32310, USA

[d] Department of Physics, Florida State University, 77 Chieftan Way, Tallahassee, FL 32306, USA

[e] Department of Chemistry, University of Tennessee, 1420 Circle Dr, Knoxville, TN 37996 USA

[f] Department of Physics, University of Tennessee, 1408 Circle Dr, Knoxville, TN 37996 USA

[g] Department of Chemical and Biomedical Engineering, FAMU-FSU College of Engineering, Tallahassee, FL 32310, USA

* Corresponding authors: mshatruk@fsu.edu; dalal@chem.fsu.edu

Abstract

A proton-transfer reaction between squaric acid (H_2sq) and 2,3-dimethylpyrazine (2,3-Me_2pyz) results in crystallization of a new organic antiferroelectric (AFE), (2,3-Me_2pyzH^+)(Hsq^-)·H_2O (**1**), which possesses a layered structure. The structure of each layers can be described as partitioned into strips lined with methyl groups of the Me_2pyzH^+ cations and strips featuring extensive hydrogen bonding between the Hsq^- anions and water molecules. Variable-temperature dielectric measurements and crystal structures determined through a combination of X-ray and neutron diffraction reveal an AFE ordering at 104 K. The phase transition is driven by ordering of protons within the hydrogen-bonded strips. Based on the extent of proton transfer, the paraelectric (PE) state can be formulated as (2,3-Me_2pyzH^+)$_2$(Hsq_2^{3-})($H_5O_2^+$), whereas the AFE phase can be described as (2,3-Me_2pyzH^+)(Hsq^-)(H_2O). The structural transition caused by the localization of protons results in the change in color from yellow in the PE state to colorless in the AFE state. The occurrence and mechanism of the AFE phase transition have been also confirmed by heat capacity measurements and variable-temperature infrared and Raman spectroscopy. This work demonstrates a potentially promising approach to the design of new electrically ordered materials by engineering molecule-based crystal structures in which hydrogen-bonded interactions are intentionally partitioned into quasi-one-dimensional regions.

Introduction

Materials that exhibit electric ordering find important technological applications in ceramic capacitors, actuators, piezoelectric transducers, pyroelectric detectors, and sonars.[1] They are also extensively investigated in the search for new types of functionality, e.g., multiferroics.[2] While this area of research has been heavily dominated by inorganic materials, especially transition metal oxides,[3] organic ferroelectrics have become much more notable since early 2000s,[4] especially due to discoveries of several remarkable

organic ferroelectric materials[5] whose performance figures of merit are comparable to those of the state-of-the-art inorganic ferroelectrics.[6]

Designing materials with electric ordering represents a non-trivial task. While phenomenologically analogous to ferro- and antiferroelectrics, magnetic materials only require sufficiently strong magnetic exchange coupling between moments on interacting magnetic sites in order to undergo magnetic ordering below the critical temperature. In contrast, ferroelectric (FE) materials require symmetry breaking in the crystal structure, with the formation of a polar space group, in order to transition from the disordered paraelectric (PE) phase to the ordered FE phase.[7] In contrast to magnetic ordering, electric ordering generally requires concerted atomic displacements to achieve the breaking of space-group symmetry.[8]

The current interest in organic FEs is justified by both the light weight of these materials and the high synthetic tunability of the molecular components that comprise them. The design of FE or antiferroelectric (AFE) organic solids generally relies on three different mechanisms: charge ordering, polar group ordering, or proton transfer. The latter is especially appealing, because the possibility of proton transfer is predictable and can occur with a high degree of cooperativity, which in turn can trigger abrupt FE or AFE ordering. A classic example of this behavior among inorganic materials is the ferroelectric transition in KH_2PO_4.[9] Among organic ferroelectrics, noteworthy cases are FE ordering in croconic acid[10] and AFE ordering in squaric acid.[11] While these organic acids represent single-component FE and AFE materials, respectively, Horiuchi and co-workers also reported a fascinating example of two-component ferroelectrics obtained by co-crystallization of organic base phenazine and haloanilic acids.[5a] This work demonstrated the predictable formation of FE materials based on the analysis of pK_a values of individual components to ensure the feasibility of proton transfer in the solid state.

Despite the potential for concerted proton displacements in co-crystals of organic acids and bases, the realm of organic FE and AFE materials remains relatively narrow, in large part due to the often unpredictable effects of crystal packing that lead to annihilation of local polarity induced by the acid-base proton transfer. Herein we demonstrate the synthesis of a new organic AFE based on the combination of squaric acid (H_2sq) and 2,3-dimethypyrazine (2,3-Me$_2$pyz). A distinct feature of this AFE material is the partitioning of molecular layers in its crystal structure into regions that feature either van-der-Waals interactions between weakly polar methyl groups or extensive hydrogen bonding, due to the asymmetric nature of the 2,3-Me$_2$pyz molecule with the respect to its N⋯N axis. We use a combination of X-ray and neutron scattering, dielectric and heat capacity measurements, and vibrational spectroscopy to elucidate the behavior of this material and the nature of the electric phase transition observed at 104 K.
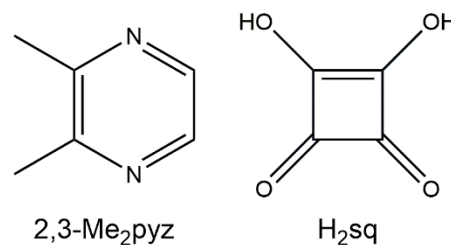
2,3-Me$_2$pyz   H$_2$sq

Experimental Section

Starting Materials. Squaric acid, H_2sq (98%, Oakwood Chemical), and 2,3-dimethylpyrazine, 2,3-Me$_2$pyz (99%, Alfa Aesar), were used as received.

(2,3-Me$_2$pyzH$^+$)(Hsq$^-$)·H$_2$O (1). H_2sq (1.00 g, 8.77 mmol) was dissolved in 10 mL of deionized water at 50 °C, and neat 2,3-Me$_2$pyz (0.96 mL, 8.77 mmol) was added dropwise to this solution, resulting in the change

2

of color from colorless to bright-yellow. The solution was cooled to room temperature, and yellow block-shaped crystals began to form within a few minutes. The solution was left undisturbed for 1 day, after which time the crystals were recovered by filtration and dried by suction. Yield = 0.86 g (43%). Anal. Calcd. (Found) for $C_{10}H_{12}N_2O_5$ (**1**): C, 50.00 (50.05); H, 5.04 (4.98); N, 11.66 (11.58).

X-ray Crystallography. Room-temperature powder X-ray diffraction (PXRD) was performed on a Panalytical XPert Pro diffractometer with $CuK\alpha$ radiation (λ = 1.54178 Å). The PXRD patterns were collected over a 2θ range of 10-60° with a step of 0.033° and 0.50 s/step counting time. The data were processed with the CrystalDiffract software.

Single-crystal X-ray diffraction (SCXRD) experiments were performed on a Bruker APEX-II CCD X-ray diffractometer equipped with a graphite-monochromated $MoK\alpha$ radiation source (λ = 0.71073 Å). A single crystal of **1** was suspended in Paratone-N oil (Hampton Research) and cooled to the desired temperature in a N_2 cold stream. The data sets were recorded as ω-scans at 0.4° step width and integrated with the Bruker SAINT software package.[12] A multi-scan empirical adsorption correction was based on multiple equivalent measurements (SADABS).[13] The space group determination was performed with XPREP,[14] and the crystal structure solution and refinement were carried out using SHELX.[15] The final refinement was performed with anisotropic atomic displacement parameters (ADPs) for all non-hydrogen atoms. The methyl and aromatic H atoms were placed in calculated positions and refined in the riding model, while the H atoms involved in hydrogen bonding were located from the difference Fourier electron density map and refined with isotropic ADPs, without restricting the N–H or O–H distances. A summary of pertinent information relating to data collection and crystal structure refinements is provided in Table 1.

Neutron Diffraction. Time-of-flight single-crystal neutron diffraction (SCND) was performed on the TOPAZ diffractometer at the Spallation Neutron Source (Oak Ridge National Laboratory). The crystal was mounted on a MiTeGen loop using a small amount of Super Glue. The data collection strategy was obtained with CrystalPlan.[16] The data were collected for ~60 h at 90 K using 44 sample orientations with 8 C of proton charge each at the beam power of 1 MW and for ~45 h at 230 K using 34 sample orientations with 6 C of proton charge each at the same beam power. Peak integration and data reduction were performed in accordance with previously reported procedures.[17] The positions of H atoms were located from the difference Fourier maps calculated using the neutron diffraction data. The crystal structures were refined anisotropically using SHELX[15] and the ShelXle graphical interface.[18] The details of data collection and crystal structure refinement are summarized in Table 1.

Table 1. Data collection and structure refinement parameters for **1** from SCXRD and SCND experiments.

Formula	$C_{10}H_{12}N_2O_5$ (**1**)				
	SCXRD			SCND	
T, K	90	230		90	230
CCDC number	1899624	1899171		1898766	1899623
Formula weight	240.22	240.22		240.22	240.22
Space group	$P\bar{1}$	$P\bar{1}$	$A\bar{1}^a$	$P\bar{1}$	$P\bar{1}$
a, Å	7.9812(6)	6.721(4)	7.967	7.981(2)	6.721(4)
b, Å	12.5493(9)	7.967(4)	12.633	12.549(3)	7.967(4)
c, Å	12.7113(9)	10.750(6)	12.723	12.711(3)	10.750(6)
α, deg	63.345(1)	76.398(5)	64.03	63.35(3)	76.398(5)
β, deg	73.512(1)	89.550(6)	73.40	73.51(3)	89.550(6)
γ, deg	83.413(1)	80.515(6)	83.35	83.41(3)	80.515(6)
V, Å^3	1090.9(1)	551.5(5)	1103.0	1090.9(5)	551.5(5)
Z	4	2	4	4	2
Crystal color	colorless	yellow		colorless	yellow
Crystal size, mm^3	0.51×0.51×0.40	0.81×0.32×0.24		3.6×1.35×0.85	3.6×1.35×0.85
d_{calc}, g cm^{-3}	1.463	1.446		1.463	1.450
μ, mm^{-1}	0.119	0.118		$0.13084 + 0.0888\lambda$	$0.12957 + 0.0879\lambda$
λ, Å	0.71073	0.71073		0.40–3.36	0.40–3.36
θ_{max}, deg	28.47	28.53		78.55	79.03
Total reflections	10012	6204		10119	5223
R_{int}	0.020	0.031		0.108	0.114
Unique reflections	4954	2557		5879	2796
Parameters refined	334	173		524	297
Restraints used	0	0		0	0
R_1, wR_2 [$I > 2\sigma(I)$]^b	0.039, 0.117	0.043, 0.104		0.084, 0.200	0.078, 0.179
R_1, wR_2 (all data)	0.051, 0.129	0.070, 0.116		0.084, 0.201	0.079, 0.179
Goodness of fit^c	1.078	1.052		1.339	1.169
Diff. peak/hole, e Å^{-3}	0.31, −0.33	0.20, −0.21		2.30, −1.51	1.02, −0.88

^{a} The alternative non-standard space group setting is provided for the high-temperature structure to afford the direct comparison to the unit cell of the low-temperature structure (see the discussion in the text). ^{b} $R_1 = \Sigma||F_o|-|F_c||/\Sigma|F_o|$; $wR_2 = [\Sigma[w(F_o^2-F_c^2)^2]/\Sigma[w(F_o^2)^2]]^{1/2}$; ^{c} Goodness-of-fit = $[\Sigma[w(F_o^2-F_c^2)^2]/(N_{obs}-N_{params})]^{1/2}$, based on all data.

Dielectric Measurements. A single crystal of **1** with the size of 7×4×1.3 mm^3 was selected for measuring the dielectric constant as a function of temperature and electric polarization as a function of applied electric field. To obtain a parallel capacitor geometry, Cr/Ag contacts were deposited on two opposite flat surfaces, corresponding to the [$\bar{2}$01] and [20$\bar{1}$] faces of the crystal (these faces are parallel to the layers observed in the crystal structure, as will be described below). The deposition has to be performed very carefully, due to the delicate nature of the crystal. First, the edges of the crystal were covered with a Kapton-tape mask,

which also attached the crystal to an aluminum plate, for more efficient thermal contact with the cooling plate of the evaporator stage. The assembly was mounted in an evaporator chamber, which was subsequently evacuated for 10 s and then flushed with N_2 gas, and this process was repeated five times to minimize the amount of moisture in the chamber. To avoid deterioration of the crystal under high vacuum, the sample stage was first cooled down by liquid N_2 to –30 °C under 10^{-2} torr and then the pressure was decreased to 3×10^{-7} torr as the sample stage temperature was lowered to –110 °C. A 5-nm film of chromium followed by a 100-nm film of silver were deposited at the rate of 0.1 nm/s. The temperature of the sample stage increased to –70 °C during the evaporation. After the deposition had been completed, the chamber was flushed with N_2 gas for 20 min to warm up the sample before opening the chamber. The crystal was flipped, and the deposition process was repeated on the other side. The crystal prepared in such a way had the active electrode area of ~11 mm^2. After making electrical contacts, the assembly was covered with Apiezon-N® grease to prevent degradation of the sample and to enhance thermal coupling to the sample platform. The capacitance was measured using a capacitance bridge (Andeen-Hagerling AH2700A) at AC electric field frequencies from 0.2 to 20 kHz. The dielectric constant was obtained from the capacitance by approximating an infinite parallel capacitor geometry. The temperature was varied at a 1 K min^{-1}. The electric polarization was measured as a function of electric field at 2.5 and 200 K with the maximum applied voltage of 3 kV and 2 kV, respectively.

Thermal Analysis. Heat capacity measurements were performed on a 3.89 mg pellet of **1** in the temperature range from 300 to 2 K, using the Physical Property Measurement System (Quantum Design). Apiezon-N® grease was used to thermally couple the sample to the platform of the calorimeter. The contribution of the platform, including the grease, was measured independently and subtracted from the total heat capacity data. Simultaneous differential scanning calorimetry and thermogravimetric analysis (SDTA) was performed on a 7.52 mg powder sample of **1** contained in an alumina crucible. The measurement was carried out on a TA Instruments SDT 600Q analyzer under a 100 mL min^{-1} flow of Ar gas, in the temperature range from 300 to 873 K and at 5 K min^{-1} heating rate.

UV-Visible Spectroscopy. The spectrum was collected on a microcrystalline sample of **1** at room temperature, using an Edinburgh FLS980 spectrometer with the integrating sphere accessory. Light output from a housed 450 W Xe lamp was passed through a single grating (1800 l/mm, 250 nm blaze) Czerny-Turner monochromator and then into the integrating sphere containing the powder sample or scattering reference ($BaSO_4$). The output from the integrating sphere was passed through a single grating (1800 l/mm, 500 nm blaze) Czerny-Turner and finally detected by a Peltier-cooled Hamamatsu R928 photomultiplier tube. Synchronous spectral scans were performed with both excitation and emission monochromators, with zero wavelength offset, stepping through the pre-set spectral range. Absorbance was then calculated using Edinburgh's F900 software package.

Infrared Spectroscopy. A polycrystalline sample of **1** was mixed with KBr for transmittance Fourier transform infrared spectroscopy experiments. The measurements were performed on a Bruker Equinox 55 spectrometer equipped with a microscope and a low-profile cryostat (550 – 7500 cm^{-1}; 4.2 – 300 K). The middle infrared frequency range was examined to reveal hydrogen-bonding effects. Mode assignments were made using lattice dynamics calculations performed with Spartan, as well as by comparison with literature data. Traditional fitting techniques were employed as appropriate.

Raman Spectroscopy. Raman spectra were collected on a 1-mm thick, pelletized sample of **1**, using an Acton SP2500 spectrometer with 1200 g mm^{-1} grating and a 100 μm entrance slit, providing 3 cm^{-1} resolution. The measurements were performed in the temperature range from 30 to 150 K. The sample was mounted on a copper cold finger inside a continuous-flow He cryostat. Spectra were recorded from in the 90–3200 cm^{-1} range in quasi-backscattering geometry with non-polarized 532 nm light. A long-pass edge filter was used to attenuate elastically scattered light. A liquid nitrogen cooled Si CCDC was used for detection. The power incident of the sample was around 2 mW.

Results and Discussion

Synthesis and Stability Studies. Compound **1** was obtained by a reaction between H_2sq and 2,3-Me$_2$pyz in water in a 1:1 molar ratio. Bright-yellow X-ray quality crystals (Figure S1) grew from the obtained yellow solution within 30 min at room temperature. The typical crystals were elongated plates, with the long edge often exceeding 1 cm. The crystals are air- and moisture-stable and remain intact for prolonged periods if kept in a closed container. Upon exposure to air, 2,3-Me$_2$pyz and H_2O gradually sublime from the lattice over the course of several days, resulting in the formation of pure H_2sq. Heating a powdered sample of **1** to 50 °C under vacuum accelerates the decomposition process, producing pure H_2sq after 20 h, as confirmed by PXRD patterns recorded before and after the decomposition (Figure S2). Simultaneous differential scanning calorimetry and thermogravimetric analysis (SDTA) showed the loss of 2,3-Me$_2$pyz and H_2O beginning at room temperature and lasting till approximately 425 K, at which point 48.7% of the initial mass remained, in good agreement with the expected mass of 47.5% for the pure H_2sq residue. The remaining H_2sq is then stable until decomposition at 525 K (Figure S3).

Based on the observed behavior of **1**, its crystals were stored in capped glass vials to prevent any degradation prior to their characterization with diffraction and other physical methods.

Dielectric Properties. The temperature-dependent capacitance measurements on a single crystal of **1** were performed to extract the complex dielectric constant, $\varepsilon(\omega) = \varepsilon'(\omega) + i\varepsilon''(\omega)$. The data analysis revealed a sharp decrease in the real part (ε') of the dielectric constant below ~115 K (Figure 1), while the imaginary part (ε'') remained near zero over the entire temperature range. The anomaly in the dielectric signal did not exhibit any notable frequency dependence (Figure S4). The pyroelectric current measured near the transition temperature was negligible, and no spontaneous electric polarization was observed.
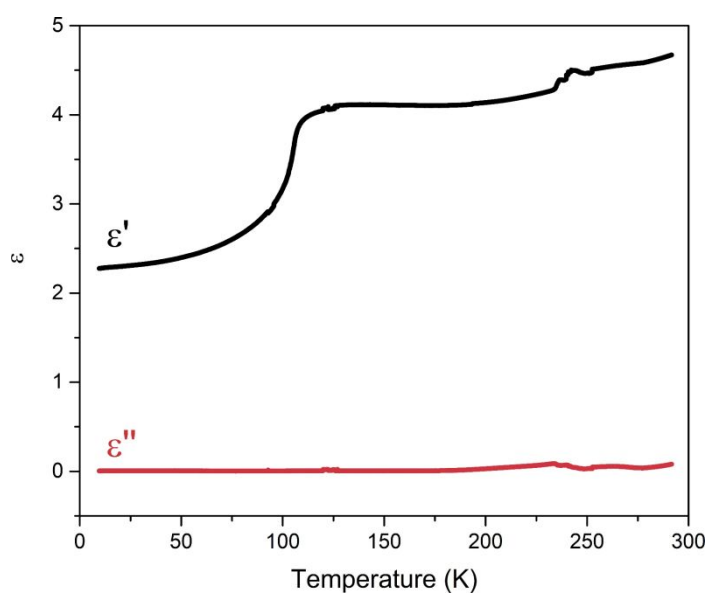
Figure 1. Temperature dependence of the real (ε') and imaginary (ε'') parts of the dielectric constant measured on a single crystal of **1** at the applied AC electric field of the amplitude 15 V and the frequency 2 kHz.

Furthermore, electric polarization measured at 2.5 K showed linear dependence on the applied electric field and the lack of hysteretic behavior (Figure S5). All these observations suggest a possible AFE phase transition,[19] which emerges from the spontaneous anti-parallel ordering of electric dipoles and leads to the decrease in the macroscopic polarizability.[20] The observation of this dielectric anomaly led us to investigate other temperature-dependent properties of this material, especially the possible changes in its crystal structure above and below the temperature of dielectric anomaly.

Crystal Structure. To elucidate the mechanism of the possible phase transition, the crystal structure of **1** was determined by a combination of SCXRD and SCND (for hydrogen atom detection) at 90 and 230 K, that is, below and above the observed decrease in the dielectric constant. At 230 K, the material crystallizes in the centrosymmetric triclinic space group $P\bar{1}$ with $Z = 2$. Upon lowering the temperature to 90 K, a super-cell with $Z = 4$ was detected, although the space group remained the same. (As will be shown below, the formation of the superstructure is due to the ordering of H atoms involved in hydrogen bonding.) The relationship between the two structures may also be expressed by considering the high-temperature structure in a non-standard base-centered space group $A\bar{1}$, obtained from the standard $P\bar{1}$ lattice by means of a transformation matrix, $\begin{pmatrix} 0 & 1 & 0 \\ -1 & 0 & 1 \\ 1 & 0 & 1 \end{pmatrix}$. This transformation results in a unit cell with $Z = 4$, with parameters and volume comparable to those of the low-temperature structure (Table 1). The structural transition leads to the loss of the A-centering, which is equivalent to the doubling of the primitive unit cell observed at 230 K.

The crystal structure of **1** is built of layers (Figure 2a), which are parallel to the $(\bar{2}01)$ planes that correspond to the basal faces of the plate-like crystals. The distance between adjacent layers is 3.092 Å. In each layer, the base and acid components alternate in such a way that one can distinguish strips lined with methyl groups alternating with strips featuring extensive hydrogen bonding (Figure 2b). One proton from each squaric acid molecule is transferred to a neighboring 2,3-Me$_2$pyz molecule, resulting in the formation of 2,3-Me$_2$pyzH$^+$ ions. The protonated side of the 2,3-Me$_2$pyzH$^+$ cations is oriented toward the region of hydrogen bonding, while the side with methyl substituents forms the methyl-lined strip. The protonated N atoms form asymmetric hydrogen bonds to the Hsq$^-$ anions, with
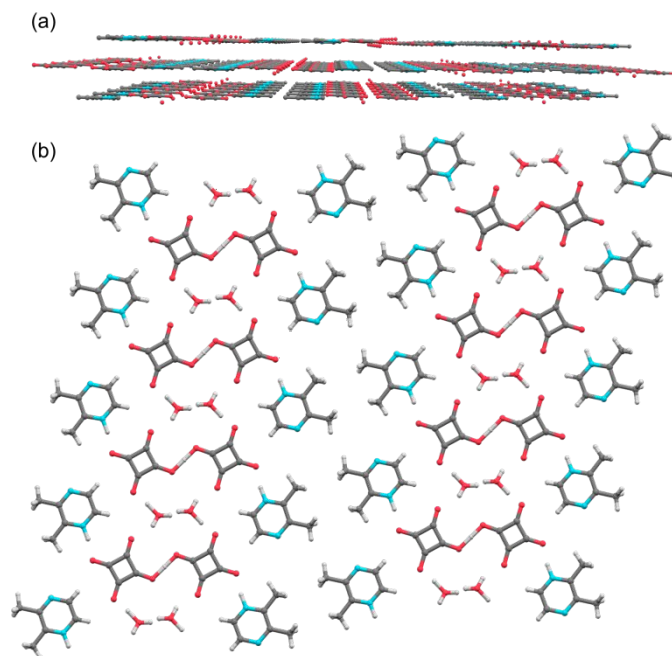
Figure 2. (a) The perspective side view of molecular layers in the crystal structure of **1** at 230 K Hydrogen atoms are omitted for clarity. (b) The idealized view of the structure of a single layer, which runs parallel to the $(\bar{2}01)$ plane, showing the separation of the structure into regions lined with methyl groups and regions of extensive hydrogen bonding. Color scheme: O = red, N = blue, C = dark gray, H = light gray.

7

the N(1)–H(1)···O(1) distance of 2.640(3) Å at 230 K. Further, the region of extensive hydrogen bonding is composed of the Hsq$^-$ anions and water molecules (Scheme 1 and Table 2). At 230 K, we observe a symmetric H-bonded dimer of the hydrosquarate anions, $(Hsq_2)^{3-}$, with the bridging proton appearing on the inversion center and the O(3)···H(3)···O(3)′ distance of 2.485(5) Å. One of the hydrosquarate protons has been transferred from this dimer to the neighbor water molecules, resulting in a protonated dimer of water molecules, $(H_5O_2)^+$. Thus, the crystal-chemical formulation of the PE phase can be represented as (2,3-Me$_2$pyzH$^+$)$_2$(Hsq$_2$$^{3-}$)(H$_5O_2$$^+$). The protonated water dimer forms asymmetric H-bonds to the adjacent $(Hsq_2)^{3-}$ dimers, with the O(5)–H(5)···O(2) distance of 2.544(4) Å. The proton H(5B), which participates in an asymmetric H-bond between water molecules with the O(5)–H(5B)···O(5)′ distance of 2.552(7) Å, is disordered over two equally occupied positions. This suggests that the protons H(2) and H(3), which are involved in H-bonding of the $(Hsq_2)^{3-}$ dimer, undergo dynamic shifts between the corresponding O atoms, so that when the H(3) proton is shifted closer to one of the hydrosquarate anions, then this anion transfers its H(2) proton closer to the water molecule, which gives up its H(5B) proton to the next water molecule, which then transfers its proton closer to the next hydrosquarate anion, which in turn causes the shift of the H(3) proton to the other hydrosquarate unit in the dimer, and so on. Such dynamic picture is additionally supported by the enlarged ADPs of the H(2), H(3), and H(5B) atoms (Figure S6a). We would like to note that the refinement of these ADPs gave reliable results with both the SCND and SCXRD data.

Upon lowering the temperature from 230 to 90 K, the distribution of protons changes substantially, as revealed by SCND. (The non-hydrogen parts of the structure obtained from SCXRD experiments were used as initial models when refining H atom parameters against SCND data.) While the proton that bridges the Hsq$^-$ anions is shared equally between them at 230 K, this local symmetry is broken at 90 K, as the proton is shifted toward one of the O atoms, forming the asymmetric O(3)–H(3)···O(3)′ bridge with O–H distances of 1.056(5) and 1.457(6) Å, respectively (Scheme 1b). The Hsq$^-$ anion that "gave up" the H(3) proton in this bonding is now observed to acquire an outer H(2) proton from the neighbor water molecule, while the Hsq$^-$ that acquired the H(3) proton transfers its outer H(2) proton to another water molecule. Accordingly, the H(5B) proton involved in H-bonding between the water molecules has become completely ordered, forming an asymmetric H-bond. The metrics of the asymmetric O(2)–H(2)···O(5), O(5)–H(2)···O(2), and O(5)–H(5B)···O(5)′ bridges can be found in Table 2. As a result of this ordered H-bonding, the SCND experiment reveal the formation of a supercell with about two times larger volume relative to the volume of the unit cell observed at 230 K.

The ordering of protons within each layer also leads to "dimerization" of the layered structure, as shorter (~2.80 Å) and longer (~3.18 Å) interplanar separations alternate in the 90 K structure, in contrast to the uniform interplanar separation of ~3.09 Å in the 230 K structure. The layers are oriented parallel to the $(\bar{2}01)$ lattice plane in the 230 K structure, which is transformed to the $(03\bar{1})$ plane in the 90 K structure.
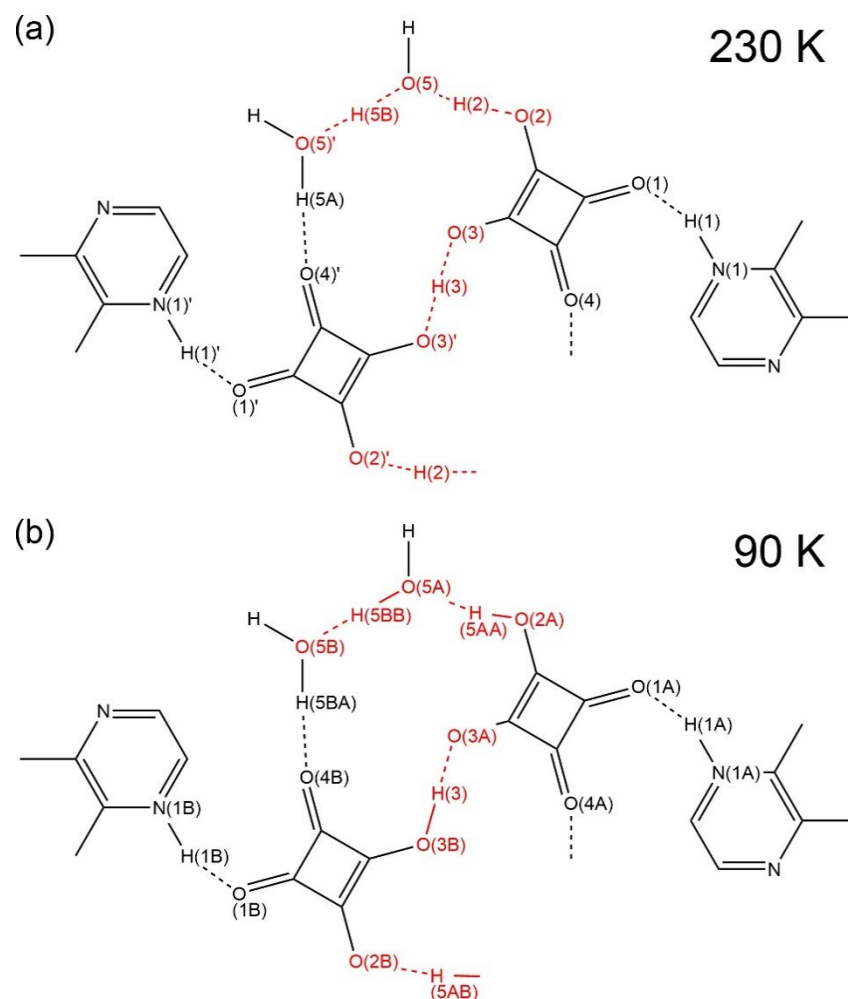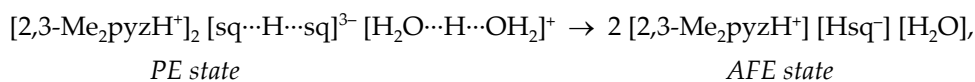
Scheme 1. Hydrogen bonding between molecular components in the crystal structure of **1** at 230 K (a) and 90 K (b). The hydrogen bonds that become ordered at lower temperatures are highlighted with red color. The crystallographic numbering is indicated only for the most important atoms involved in hydrogen bonding. The full atom numbering scheme and atomic displacement ellipsoids are provided in Figure S6.

Table 2. Distances between atoms involved in hydrogen bonding in the structure of **1** from SCND. The labels B and A indicate the N and/or O atoms involved in the hydrogen-bonding pairs.

| Hydrogen bond	d(B–A), Å		d(B–H), Å		d(H···A), Å	
(B–H···A)	90 K	230 K	90 K	230 K	90 K	230 K
N(1)–H(1)···O(1)	2.625(3) 2.655(3)	2.640(3)	1.080(5) 1.093(5)	1.095(5)	1.583(6) 1.536(6)	1.549(5)
O(3)–H(3)···O(3)′	2.512(6)	2.485(5)	1.056(8)	1.243(3)	1.457(9)	1.243(2)
O(5)–H(2)···O(2)	2.445(4) 2.677(5)	2.544(4)	1.339(8) 0.994(7)	1.090(9)	1.111(8) 1.685(7)	1.458(9)
O(5)–H(5B)···O(5)′	2.569(6)	2.552(7)	1.552(8)	0.92(1)	1.018(8)	0.92(1)
O(5)–H(5A)···O(4)	2.651(6) 2.709(6)	2.669(5)	0.982(9) 0.986(9)	0.985(7)	1.76(1) 1.821(1)	1.783(7)

An examination of the crystal packing in the 90-K crystal structure reveals that the protons are shifted in a concerted fashion within the hydrogen-bonded region, producing a net in-plane dipole moment, while the protons of the next hydrogen-bonded region shift to produce a dipole moment in the opposite direction (Figure S7). Thus, because of the structural phase transition, net dipole moments formed in the adjacent hydrogen-bonded regions cancel each other, which explains the observed drop in the dielectric constant and suggests the occurrence of an AFE phase transition. The proton re-distribution can also be described with the following reaction scheme:

$$[2,3\text{-Me}_2\text{pyzH}^+]_2\ [\text{sq}\cdots\text{H}\cdots\text{sq}]^{3-}\ [\text{H}_2\text{O}\cdots\text{H}\cdots\text{OH}_2]^+\ \rightarrow\ 2\ [2,3\text{-Me}_2\text{pyzH}^+]\ [\text{Hsq}^-]\ [\text{H}_2\text{O}],$$

$$PE\ state \qquad\qquad\qquad\qquad\qquad AFE\ state$$

where the high-temperature PE state features delocalized protons in the hydrogen-bonded dimers, Hsq_2^{3-} and H_5O_2^+, while the low-temperature AFE state contains only localized protons.

Such description of the PE→AFE phase transition also justifies the change in color from yellow in the PE state (Figures S1 and S8) to colorless in the AFE state. Based on reported calculations of the electronic structure of squaric acid and pyrazine derivatives,[21] we expect the highest occupied molecular orbitals, HOMO and HOMO–1, to be represented by π-orbitals of 2,3-Me$_2$pyzH$^+$ and the lowest unoccupied molecular orbitals, LUMO and LUMO+1, to correspond to π*-orbitals of Hsq$^-$, and the lowest-energy optical absorption bands correspond to charge transfer from HOMO/HOMO–1 to LUMO/LUMO+1. The involvement of the Hsq$^-$ anions in delocalized hydrogen bonding should lower the energy of LUMO and LUMO+1, while the loss of such delocalization will have an opposite effect, shifting the absorption bands completely to the UV region, which explains the loss of color by crystals of **1** in the AFE phase.

Thermodynamics of the Phase Transition. Heat capacity (C_p) measurements revealed a broad anomaly in the region of the structural phase transition (Figure 3). The change in entropy due to this phase transition, $\Delta S_t = \int \frac{\Delta C_p}{T}dT$, was found by numerical integration of the C_p/T vs. T curve after subtracting a baseline extrapolated from the regions above and below the C_p anomaly (Figure 5, inset). The procedure resulted in ΔS_t = 0.55 J mol^{-1} K^{-1}. Based on the Boltzmann-Planck formula, $\Delta S_t = R\ln N$, where R is the ideal gas constant and N is the ratio of possible states in the high-temperature phase to those in the low-temperature phase, values of $N = 2$ and ΔS_t = 5.76 J mol^{-1} K^{-1} are expected for an ideal two-fold order-disorder phase transition. The significantly smaller experimental value of ΔS_t suggests that the mechanism of this AFE phase transition cannot be thought
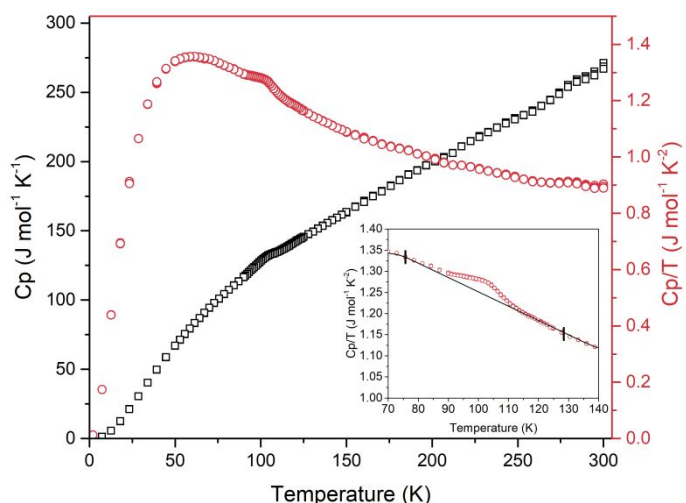

Figure 3. The temperature dependence of C_p and C_p/T measured on a pelletized powder sample of **1**. The black line in the inset shows the extrapolated baseline, while the vertical black lines mark the beginning and end points of the integrated region.

10

of as the simple ordering of protons. Previous studies of the heat capacity anomaly around the AFE phase transition temperature in pure H_2Sq found $\Delta S_t = 0.228$ J mol^{-1} K^{-1}, which similarly deviates from the value of 11.28 J mol^{-1} K^{-1} expected for two protons ordering per molecular unit.[22] Based on investigation of isotope-dependent effects on the FE transition in KH_2PO_4, it was proposed that the suppression of the experimentally determined values ΔS_t might be due to tunneling terms unaccounted by the simple Boltzmann-Planck model.[23] The suppression of the ΔS_t value might also stem from glassy effects in the phase transition. In the present case, however, such effects are negligible, because the dielectric signal at the phase transition does not show any dissipation, as can be judged from the near-zero value of the out-of-phase dielectric constant (Figure 1a).

Vibrational Spectroscopy. Raman spectra collected over the 30–150 K temperature range (Figure 4a) resemble a combination of the spectra for pure H_2Sq[24] and 2,3-Me_2pyz,[25] allowing straightforward assignment of the vibrational bands (Table S2). The positions of all observed peaks are essentially independent of temperature, suggesting the structural phase transition does not impact the strength of intramolecular bonds. Several peaks, however, exhibit significant decrease in the full-width at half-maximum (FWHM) as the temperature is lowered (Figure 4b), indicating an increased ordering of atomic positions associated with these frequencies. In particular, the FWHM of the band assigned to $\delta(C'O')$ A_1 in squaric acid follows the phase transition seen in the dielectric measurements. The bands assigned to the 2,3-Me_2pyz moieties, in general, lack similar temperature dependence of the FWHM (Figure 4c), with the exception of the 1260 cm^{-1} band, the intensity of which varied greatly due to the broad underlying absorption feature observed in the corresponding region at lower temperatures (Figure 4a).
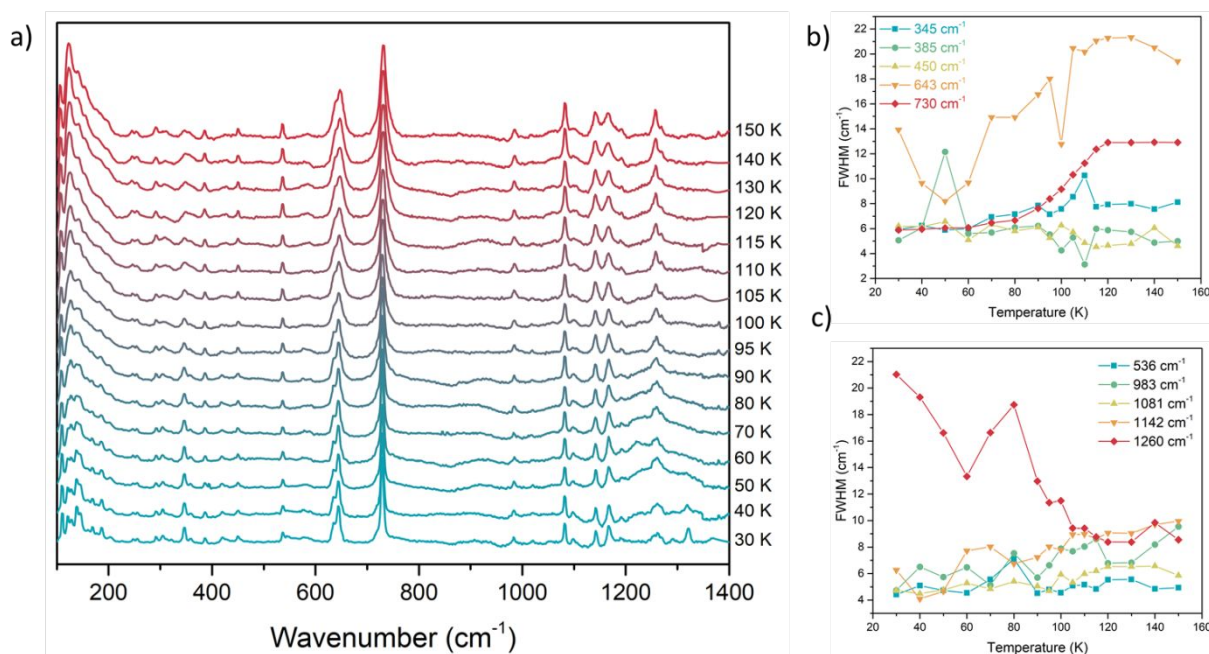
Figure 4. Variable temperature Raman spectra of **1** collected between 30 and 150 K (a) and temperature dependence of the FWHM for peaks assigned to the H_2sq fragments (b) and the 2,3-Me_2pyz fragments (c).
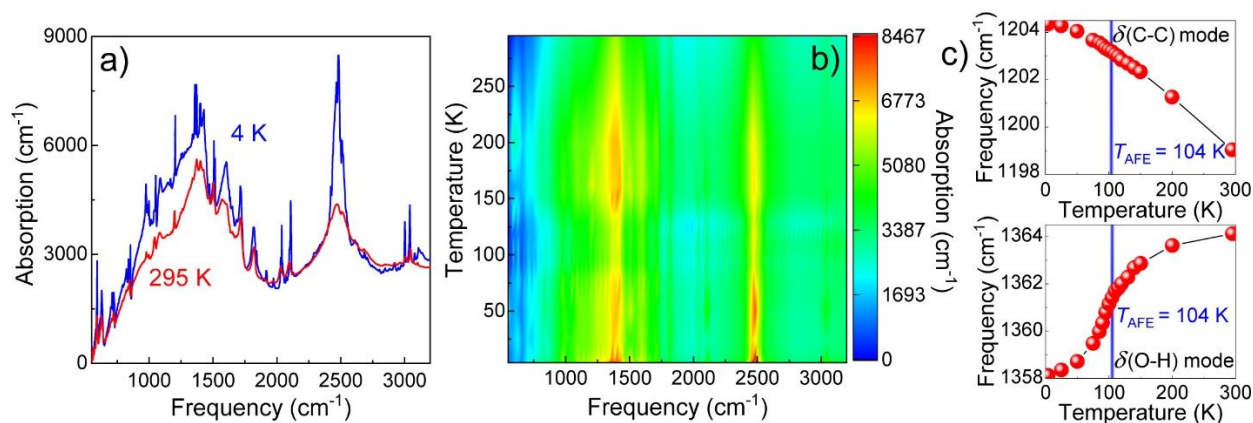
Figure 5. (a) Middle-infrared spectrum of **1** at 300 and 4.2 K. (b) Contour plot of the infrared response of **1** as a function of temperature highlighting linewidth effects across the 104 K transition. (c) Infrared frequency vs. temperature plots for the ν(C′-C′) and δ(O-H) vibrational modes (see the text for detailed discussion).

The infrared response of **1** was also examined as a function of temperature. Similar to the Raman spectra, the vibrational modes derive from the H_2Sq[24] and 2,3-Me$_2$pyz[25] building block molecules. The room-temperature spectrum also shows a strong charge transfer band centered at 1400 cm^{-1} (Figure 5a). Additional evidence for assignment of the broad structure as a low-energy charge transfer band comes from the derivative-like (Fano) lineshape of the superimposed vibrational modes.[26] The charge transfer band gains oscillator strength with decreasing temperature. Examination of the contour plot (Figure 5b) reveals that the charge transfer band narrows across the PE→AFE phase transition temperature (T_{AFE}). These linewidth changes – on the order of 10% – recover fully away from T_{AFE}. At the same time, the vibrational features sharpen with decreasing temperature. Vibrational linewidth trends are consistent with decreasing thermal fluctuations, as evidenced by the Raman scattering and thermal ellipsoid behavior already discussed in the text, with a distinct narrowing near the 104 K AFE transition (Figure 5b).

We also should point out that several of the vibrational modes soften with decreasing temperature. This is a common signature of enhanced hydrogen bonding.[27] As an example, we track two different vibrations associated with H_2Sq as a function of temperature. The A_1 symmetry δ(O-H) mode softens with decreasing temperature (Figure 5c). The softening may also be connected to the symmetric ↔ asymmetric positioning of the H atom in the O···H···O pathway. Three other vibrational modes – the B_1 symmetry π(O-H), B_2 symmetry δ(O-H), and B_2 symmetry $ν_{as}$(C′=O′) at 977, 1375, and 1822 cm^{-1}, respectively, – follow the same trend, suggesting that they are also involved in hydrogen-bond aided proton transfer in the structure of **1**. In contrast, the upper panel of Figure 7c displays the position of the A_1 symmetry ν(C′-C′) mode of H_2Sq as a function of temperature. The low temperature hardening is a typical anharmonic response, and there is no sensitivity to T_{AFE} within our resolution. The majority of H_2Sq[24] and 2,3-Me$_2$pyz[25] modes behave similarly, suggesting that they do not play a major role in the proton transfer in this system.

Concluding Remarks

The co-crystallization of 2,3-Me$_2$pyz and H$_2$sq provides a remarkable example of an AFE ordered phase. The asymmetric nature of the 2,3-Me$_2$pyz molecule with respect to the N···N axis forces the partitioning of

the resulting layered structure of (2,3-Me$_2$pyzH$^+$)(Hsq$^-$)·H$_2$O (**1**) into regions lined with methyl groups and regions that feature extensive hydrogen-bonded interactions between deprotonated Hsq$^-$ anions and co-crystallized water molecules. The presence of these hydrogen-bonded regions eventually leads to the spontaneous AFE ordering at 104 K. The phase transition was conclusively confirmed by the combination of neutron and X-ray diffraction, dielectric and heat capacity measurements, and vibrational spectroscopy. The nature of the crystal structure of **1** and the mechanism of AFE ordering hint at a potentially promising approach to the design of new organic ferro- or antiferroelectrics. Other acid-base combinations can be explored, featuring components conducive to the separation of the structure into regions with distinctly different character of intermolecular interactions, whereas the size of the substituents on the molecular components can be systematically varied to arrive at different compositions and structural topologies. Efforts in this direction are currently under way in our laboratories.

Notes

Present address: Department of Physics, Astronomy, and Materials Science, Missouri State University, 901 S National Ave, Springfield, MO 65897, USA.

Supporting Information

The Supporting Information is available free of charge on the ACS Publications website at DOI: 10.1021/jacs.??????: a single crystal of **1** at room temperature, PXRD patterns of **1** before and after heating under vacuum, SDTA curves, the temperature- and frequency-dependent real part of the dielectric constant, additional crystal structure plots, the UV-visible spectrum, the hydrogen-bonding parameters from SCXRD experiments, and the assignment of vibrational modes.

Acknowledgments

References

1.   Scott, J. F. Applications of modern ferroelectrics. *Science* **2007**, *315*, 954-959; (b) Lines, M. E.; Glass, A. M. *Principles and Applications of Ferroelectrics and Related Materials*. Oxford University Press: Oxford, UK, 2000; 688 pp.

2. Cheong, S. W.; Mostovoy, M. Multiferroics. A magnetic twist for ferroelectricity. *Nat. Mater.* **2007**, *6*, 13-20; (b) Eerenstein, W.; Mathur, N. D.; Scott, J. F. Multiferroic and magnetoelectric materials. *Nature* **2006**, *442*, 759-765; (c) Fiebig, M.; Lottermoser, T.; Meier, D.; Trassin, M. The evolution of multiferroics. *Nat. Rev. Mater.* **2016**, *1*, 16046.

3. Granger, P.; Parvulescu, V. I.; Prellier, W., *Perovskites and Related Mixed Oxides*. Wiley-VCH: Weinheim, 2016; 978 pp.; (b) Liu, H.; Yang, X. A brief review on perovskite multiferroics. *Ferroelectrics* **2017**, *507*, 69-85; (c) Wu, H.; Xia, W.; Xue, P.; Zhu, X. Perovskite oxide nanocrystals: Synthesis, characterization, physical properties, and applications. *Ferroelectrics* **2017**, *518*, 127-136.

4. Horiuchi, S.; Tokura, Y. Organic ferroelectrics. *Nat. Mater.* **2008**, *7*, 357-366.

5. Horiuchi, S.; Kumai, R.; Tokura, Y. Room-temperature ferroelectricity and gigantic dielectric susceptibility on a supramolecular architecture of phenazine and deuterated chloranilic acid. *J. Am. Chem. Soc.* **2005**, *127*, 5010-5011; (b) Horiuchi, S.; Ishii, F.; Kumai, R.; Okimoto, Y.; Tachibana, H.; Nagaosa, N.; Tokura, Y. Ferroelectricity near room temperature in co-crystals of nonpolar organic molecules. *Nat. Mater.* **2005**, *4*, 163-166; (c) Horiuchi, S.; Kumai, R.; Tokura, Y. A supramolecular ferroelectric realized by collective proton transfer. *Angew. Chem. Int. Ed.* **2007**, *46*, 3497-3501; (d) Szafrański, M.; Katrusiak, A.; McIntyre, G. J. Ferroelectric order of parallel bistable hydrogen bonds. *Phys. Rev. Lett.* **2002**, *89*, 215507; (e) Katrusiak, A.; Szafrański, M. Disproportionation of pyrazine in $NH^{+}\cdots N$ hydrogen-bonded complexes: new materials of exceptional dielectric response. *J. Am. Chem. Soc.* **2006**, *128*, 15775-15785.

6. Horiuchi, S.; Kobayashi, K.; Kumai, R.; Ishibashi, S. Proton tautomerism for strong polarization switching. *Nat. Commun.* **2017**, *8*, 14426.

7. Litvin, D. B. Ferroelectric space groups. *Acta Crystallogr. Sect. A* **1986**, *42*, 44-47.

8. Shi, P.-P.; Tang, Y.-Y.; Li, P.-F.; Liao, W.-Q.; Wang, Z.-X.; Ye, Q.; Xiong, R.-G. Symmetry breaking in molecular ferroelectrics. *Chem. Soc. Rev.* **2016**, *45*, 3811-3827.

9. Kobayashi, K. K. Dynamical theory of the phase transition in potassium dihydrogen phosphate-type ferroelectric crystals. *J. Phys. Soc. Jpn.* **1968**, *24*, 497-508.

10. Horiuchi, S.; Tokunaga, Y.; Giovannetti, G.; Picozzi, S.; Itoh, H.; Shimano, R.; Kumai, R.; Tokura, Y. Above-room-temperature ferroelectricity in a single-component molecular crystal. *Nature* **2010**, *463*, 789-792.

11. Feder, J. Two dimensional ferroelectricity. *Ferroelectrics* **1976**, *12*, 71-84.

12. *SMART and SAINT*. Bruker AXS Inc.: Madison, WI, USA, 2007.

13. Sheldrick, G. M. *SADABS*. University of Göttingen: Göttingen, Germany, 1996.

14. Sheldrick, G. M. *XPREP. Space group determination and reciprocal space plots*. Siemens Analytical X-ray Instruments: Madison, WI, USA, 1991.

15. Sheldrick, G. M. Crystal structure refinement with SHELXL. *Acta Crystallogr. Sect. C* **2015**, *71*, 3-8.

16. Zikovsky, J.; Peterson, P. F.; Wang, X.-P. P.; Frost, M.; Hoffmann, C. CrystalPlan: An experiment-planning tool for crystallography. *J. Appl. Crystallogr.* **2011**, *44*, 418-423.

17. Schultz, A. J.; Jorgensen, M. R. V.; Wang, X.; Mikkelson, R. L.; Mikkelson, D. J.; Lynch, V. E.; Peterson, P. F.; Green, M. L.; Hoffmann, C. M. Integration of neutron time-of-flight single-crystal Bragg peaks in reciprocal space. *J. Appl. Crystallogr.* **2014**, *47*, 915-921.

18. Hübschle, C. B.; Sheldrick, G. M.; Dittrich, B. ShelXle: a Qt graphical user interface for SHELXL. *J. Appl. Crystallogr.* **2011**, *44*, 1281-1284.

19. Jain, P.; Dalal, N. S.; Toby, B. H.; Kroto, H. W.; Cheetham, A. K. Order-disorder antiferroelectric phase transition in a hybrid inorganic-organic framework with the perovskite architecture. *J. Am. Chem. Soc.* **2008**, *130*, 10450-10451.

20. Dalal, N. S.; Gunaydin-Sen, O.; Bussmann-Holder, A. Experimental evidence for the coexistence of order/disorder and displacive behavior of hydrogen-bonded ferroelectrics and antiferroelectrics. *Struct. Bonding* **2007**, *124*, 23-50.

21. Korkmaz, U.; Uçar, İ.; Bulut, A.; Büyükgüngör, O. Three forms of squaric acid with pyrazine and pyridine derivatives: an experimental and theoretical study. *Struct. Chem.* **2011**, *22*, 1249-1259.
22. Barth, E.; Helwig, J.; Maier, H. D.; Müser, H. E.; Petersson, J. Specific heat of the two dimensional antiferroelectric squaric acid. *Z. Phys. B* **1979**, *34*, 393-397.
23. Blinc, R.; Svetina, S. Cluster approximations for order-disorder-type hydrogen-bonded ferroelectrics. II. Application to KH_2PO_4. *Phys. Rev.* **1966**, *147*, 430-438.
24. Baglin, F. G.; Rose, C. B. The infrared and Raman spectra of crystalline squaric acid. *Spectrochim. Acta A* **1970**, *26*, 2293-2304; (b) Ito, M.; West, R. New aromatic anions. IV. Vibrational spectra and force constants for $C_4O_4^{-2}$ and $C_5O_5^{-2}$. *J. Am. Chem. Soc.* **1963**, *85*, 2580-2584.
25. Endrédi, H.; Billes, F.; Keresztury, G. Revised assignment of the vibrational spectra of methylpyrazines based on scaled DFT force fields. *J. Mol. Struct. Theochem* **2004**, *677*, 211-225.
26. Musfeldt, J. L.; Kamarás, K.; Tanner, D. B. Infrared studies of the phase transition in the organic charge-transfer salt *N*-propylquinolinium ditetracyanoquinodimethane. *Phys. Rev. B* **1992**, *45*, 10197-10205.
27. Jones, B. R.; Varughese, P. A.; Olejniczak, I.; Pigos, J. M.; Musfeldt, J. L.; Landee, C. P.; Turnbull, M. M.; Carr, G. L. Vibrational properties of the one-dimensional, *S* = 1/2, Heisenberg antiferromagnet copper pyrazine dinitrate. *Chem. Mater.* **2001**, *13*, 2127-2134.

TOC Graphics

230 K (Paraelectric)

$T_N = 104$ K

90 K (Antiferroelectric)